Materials Today Physics 31 (2023) 101000

Contents lists available at ScienceDirect

Materials Today Physics

journal homepage: www.journals.elsevier.com/materials-today-physics

Space-resolved light emitting and lasing behaviors of crystalline perovskites upon femtosecond laser ablation

Rahul A. Rajan [a,c], Huang Tao [a,c], Weili Yu [a,c,**], Jianjun Yang [a,b,c,*]

[a] GPL Photonics Laboratory, State Key Laboratory of Luminescence and Applications, Changchun Institute of Optics, Fine Mechanics and Physics, Chinese Academy of Science, Changchun, Jilin, 130033, P. R. China
[b] Center of Materials Science and Optoelectronics Engineering, University of Chinese Academy of Sciences, 100049, Beijing, China
[c] University of Chinese Academy of Sciences Beijing, 100049, China

ARTICLE INFO

Keywords:
femtosecond laser ablation
perovskite laser
photoluminescence
single crystal perovskite
thin film perovskite

ABSTRACT

Femtosecond laser processing of lead halide perovskites has recently sparked wide popularity for creating various micro/nanostructures and instigating interesting properties. However, it is still lacking detailed insights into correlating the laser induced morphology and defect chemistry of perovskite materials to their light emitting properties. Here, the space-resolved photoluminescence and lasing behaviors are investigated for both the single crystal (SC) and polycrystalline (PC) perovskites upon femtosecond laser ablation. In the case of SC sample, three different regions based on the laser ablation, recast deposition, and modification respectively exhibits distinguished carrier recombination mechanisms due to their variable defect chemistries and morphologies identified, which helps to realize the amplified spontaneous emission with the recrystallized micro/nanostructures. On the other hand, the laser modified region on the PC sample reveals the significant enhancement of random lasing performance (the lasing threshold was reduced by ~7 times and the slope efficiency increased by ~1.5 times), which is attributed to the femtosecond laser induced non-radiative defect passivation and the average crystalline grain size reduction by more than 1.5 times. This study unveils the physical and chemical modification effects of the femtosecond laser irradiation on perovskite materials, and thus is an optimal strategy to fabricate desired perovskite light-emitting microstructures by ultrafast laser processing.

1. Introduction

In recent years organic-inorganic halide perovskites $MAPbX_3$ (MA = CH_3NH_3, X = Br, I, and Cl) attract worldwide attention as promising active materials for applications of light-emitting and solar cells [1–9]. In general, they promise wide valuable applications in solid-state lighting, optical data encryption, multi-color displays and laser sources by relying on multiple advantages such as their large gain coefficient, easy tuning of the wavelength emission across the visible spectrum, high photoluminescence (PL) yield and facile solution processing synthesis techniques [10–14]. At the same time, the research progresses achieved in femtosecond laser ablation allows the simple, chemically clean and high-throughput micro/nano-structuring of both the single crystal (SC) and polycrystalline (PC) perovskite materials [15–19]. Irrespective of the material heterogeneity, a highly focused laser beam was known to facilitate the fabrication of micro-grooves, micro/nano-wires, rings, etc. for optoelectronics and photonics [15,20,21,22–24], which can be widely employed as various optical confinement cavities [22,25,26–28] and PL enhancing structures [29,30]. As a matter of fact, because of the Gaussian distribution of the laser pulse intensity, the induced modifications on both the geometric profile and the chemistry of the surface structure usually become space-dependent [31,32], leading to the spatial heterogeneity in optoelectronics properties of the perovskite samples [16]. Primarily, the spatial heterogeneity of light emission from the laser ablated structures indicates that there exist multiple recombination channels, including different optically active defect states [33]. Therefore, a thorough understanding of the space-resolved laser-induced effects and optical

* Corresponding author. GPL Photonics Laboratory, State Key Laboratory of Luminescence and Applications, Changchun Institute of Optics, Fine Mechanics and Physics, Chinese Academy of Science, Changchun, Jilin, 130033, P. R. China.
** Corresponding author. GPL Photonics Laboratory, State Key Laboratory of Luminescence and Applications, Changchun Institute of Optics, Fine Mechanics and Physics, Chinese Academy of Science, Changchun, Jilin, 130033, P. R. China.
E-mail addresses: weili.yu@ciomp.ac.cn (W. Yu), jjyang@ciomp.ac.cn (J. Yang).

https://doi.org/10.1016/j.mtphys.2023.101000
Received 17 December 2022; Received in revised form 20 January 2023; Accepted 28 January 2023
Available online 4 February 2023

properties across the laser-ablated structures is necessary for realizing efficient light-emitting devices.

To unveil the underlying mechanisms of PL emission and its enhancement of perovskite materials a great number of studies have been carried out. For instance, de Quintettes et al. reported that the PL intensities of adjacent grains in a homogenous film of $MAPbI_{3-x}Cl_x$ can be differed by up to 30%. By correlating the time-resolved PL (TRPL) with the confocal PL and the scanning electron microscope (SEM), the authors demonstrated that the grain structures with the higher trap density would like to increase non-radiative pathways. In specific, both the lower PL intensity and the shorter PL lifetimes of grain boundaries are attributed to their defect-rich chemistry and resultant non-radiative recombination [33]. Recently, Makarov and co-workers investigated the morphology-controlled PL enhancement and the lasing behavior from various micro/nanostructures fabricated via femtosecond laser lithography [15]. Besides, Xing et al. reported the surface modification of $MAPbBr_3$ by virtue of femtosecond laser to improve the PL intensity [34], which is mainly attributed to the texture based photon recycling and light outcoupling processes. Whereas a comprehensive understanding of the physical correlations among different effects, such as the ultrashort laser induced structural modification, defect chemistry change, carrier recombination mechanisms, and output PL and ASE/-lasing properties of perovskite materials, are still lacking.

In this paper, we found that the nonlinear interaction of femtosecond laser pulses induced the non-uniform material chemistry and crystalline modification to spatially modulate the light emitting behavior of the samples. We investigate the PL, amplified spontaneous emission (ASE) and lasing emission behaviors across the laser-ablated structures on the SC and PC perovskite samples, with the change in both material chemistry and surface morphology. The space resolved steady-state and TRPL studies along with the SEM images reveal that the laser affected (including the serious ablation, the recast deposition and the laser modification) and unaffected regions comprise distinguishable carrier recombination mechanisms by gaining different sample morphology

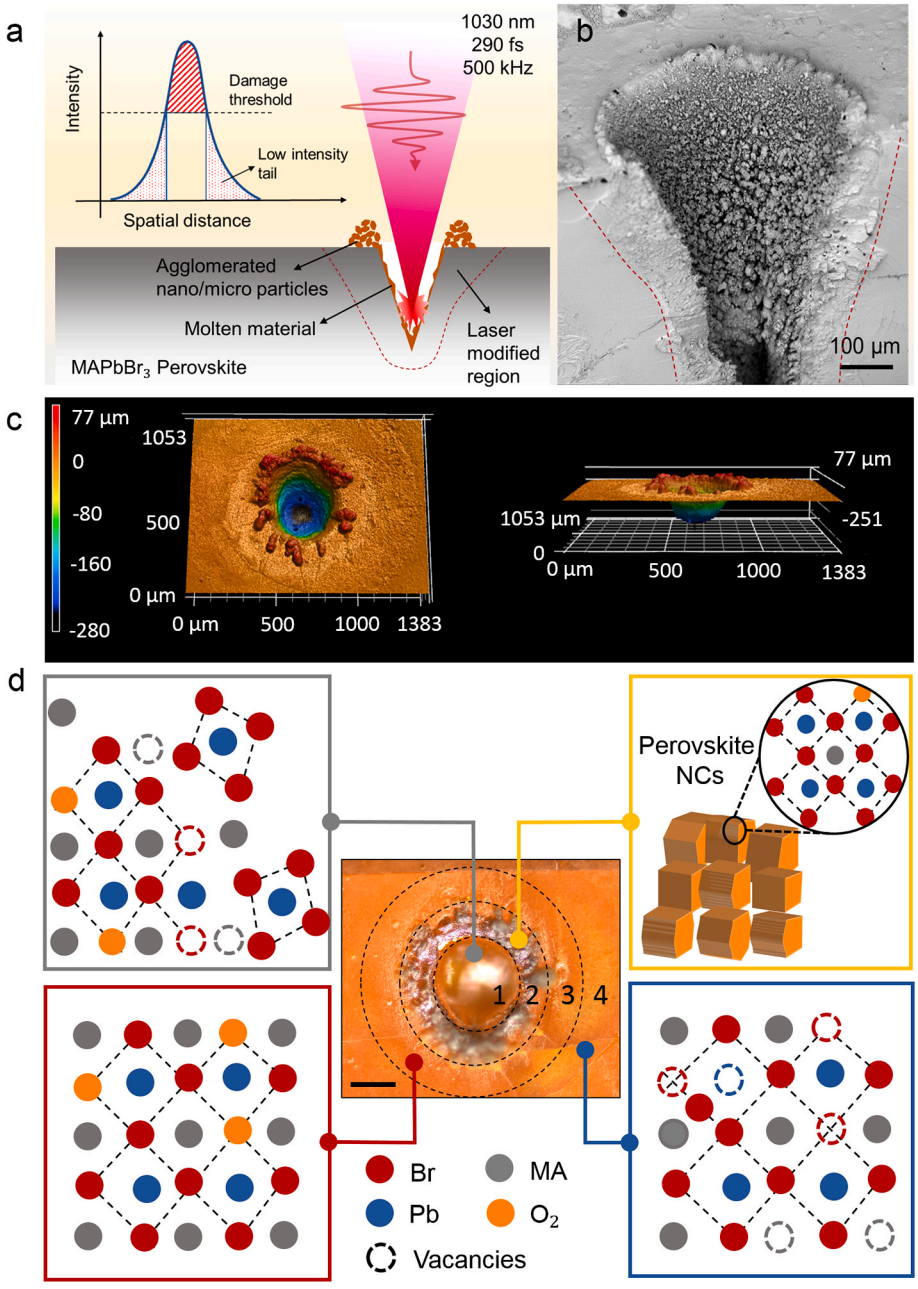

Fig. 1. (a) A schematic of the femtosecond laser interaction with $MAPbBr_3$ perovskite sample. (b) Cross-section image of the ablated crater upon femtosecond laser irradiation, where the laser modified and unaffected regions are seperated by the dotted lines. (c) Confocal microscope images of the surface morphology with the depth information of ablated crater on $MAPbBr_3$ SC. (d) Different regions on the sample surface after femtosecond laser irradiation (scale bar, 100 μm) and the corresponding perovskite crystal models, where (1) represents the ablated region with highly deformed perovskite crystals, (2) for the recast deposited region containing abundant recrystallized perovskite nanocrystals, (3) for the laser modified region consisting of perovskite crystals with less defects and deformation, and (4) depicts the unaffected region with intrinsic crystalline defect structures.

and defect chemistry. Among them, the recast deposition region that comprises many recrystallized micro/nanocrystals exhibits ASE properties. On the other hand, the laser modified regions for both the SC and PC perovskite samples shows significant defect passivation and reduced average grain size (in thin films), which consequently enhance the PL intensity and the random lasing (RL) properties. The reduction of average grain sizes can increase the multiple scattering mediated by the grain boundaries. Owing to the passivation of bulk defects, a major quick non-radiative decay pathway is cured and the excited carrier lifetime is prolonged, thus improving the light amplification by the stimulated emission even with a minimal pump fluence.

2. Results and discussion

2.1. Femtosecond laser processing of $MAPbBr_3$ perovskite crystals

We used $MAPbBr_3$ SC and PC film of cubic $Pm\ \overline{3}\ m$ space group at room temperature for processing with femtosecond laser pulses (the detailed information on the femtosecond laser system and the ablation process are given in the experimental section). Fig. 1a shows a schematic of ablating $MAPbBr_3$ perovskite material by the femtosecond laser beam, wherein the incident TEM_{00}-mode laser wavelength is $\lambda = 1030$ nm, associated with the pulse width of $\tau = 290$ fs and the repetition rate of $f_{treat} = 500$ kHz.

Through this study, we tried to deeply understand various steps of femtosecond laser-perovskite material interaction, which are described in the following. (i) Optical absorption: it is widely known that the absorption onset of $MAPbBr_3$ perovskite materials occurs at around 532 nm, with an excellent absorption coefficient of 10^4 cm^{-1} [34]. This allows the sample to absorb 1030 nm wavelength of the laser pulses through a two-photon process. (ii) Material ablation: for the incidence of a spatially Gaussian-profiled laser pulse, only the high intensity part is absorbed by the sample to initiate the ablation process (as shown in Fig. 1a); whereas the tail portions are possible to act with the sample without the ablation process because their intensities less than the damage threshold of the material. The change of surface morphology upon femtosecond laser irradiation is shown in Fig. 1b, where the SEM image shows the cross-section of an ablated crater on the single-crystal $MAPbBr_3$ perovskite. (iii) Melting and recrystallization followed by agglomeration of nanostructures: the laser-ablated surface shows the characteristic features of the high-repetition-rate laser ablation of the organic-inorganic material, which contains melted and re-crystallized traces at the center of the irradiation area and micro/nano-particle depositions along the crater edges. The center region of the laser-exposed perovskite surface partly undergoes chemical decomposition due to the heat accumulation from the high repetition rate of laser pulse irradiation [35], which consequently develops into abundant molten material profiles. In short, the observed surface morphology was the result of decomposed organic components of $MAPbBr_3$, melting, and agglomerating of the remaining inorganic materials around the ablated crater. (iv) Chemical and physical modification: some area around the crater is noticeably modified upon femtosecond laser irradiation, which might be due to the combined effect of the laser-induced heat accumulation and pressure (marked by a dotted line).

Subsequently, the three-dimensional information for the surface morphology of the laser-ablated crater was analyzed using a confocal laser scanning microscope (shown in Fig. 1c). A crater with a diameter of around 500 μm and 240 μm in depth is formed on the single-crystal sample for continuous irradiation of less than 2 s under the laser energy fluence of $F = 38.20$ μJ/cm^2. The agglomerated micro/nanocrystals were deposited around the crater edge with a height of 77 μm above the surface. In the case of the single pulse irradiation, the spot diameter is observed at ~200 μm, which can be attributed to the direct material ablation by the shock-like energy deposition alone when the laser pulse intensity is higher than the damage threshold (see Fig. 1a) [36]. Whereas, in the case of multi-pulse irradiation with a high repetition rate, the ablation process in the perovskite material with low thermal conductivity highly depends on the unavoidable incubation effect [35, 37], hence reducing the damage threshold of the material. Eventually, the ablated crater size will be larger than the laser spot size resulting from the single pulse ablation. The dimension of such craters can be varied by tuning the incident laser parameters (detailed information on single-crystal synthesis and femtosecond laser processing procedures is given in the experimental section).

Based on the laser-induced modification, the sample surface is divided into four regions as shown in Fig. 1d. Due to the Gaussian-profiled laser intensity distribution, the center region of the laser beam was seriously ablated (where the laser pulse intensity exceeds the damage threshold of the material). The imparted energy diffuses through the perovskite crystal and breaks the bonds in the organic components like MA, which leads to the deformation of the whole crystalline structure (as shown by the crystal model of Fig. 1d (1)). Upon the femtosecond laser ablation, the ejected micro/nanoparticles and molten-recrystallized traces were deposited around the ablation crater, which can be considered as the recast deposition region. Recent reports showed that the recrystallized nanocrystals exhibit better crystalline quality with reduced crystalline defects (as represented by the crystal model of Fig. 1d (2)) [38]. The low-intensity pulse tails with their heating effect can modify the material surface around hundreds of μm in radius, which is here called the laser modified region. During this lower laser intensity interaction under the atmospheric oxygen, halogen vacancies in the metal halide perovskites are getting passivated with the adsorbed or diffused oxygen through the lattice, which can enhance the overall crystalline quality and optical performance (see the crystal model in Fig. 1d (3)) [39]. We analyzed the sample surface using Energy dispersive X-ray (EDX) to check the presence of oxygen atoms in the laser induced regions (see Figure S1). It should be noted that the concentration of Pb shows a clear reduction and oxygen shows a clear increment in the laser treated regions. It confirms the existence of oxygen atoms in the laser treated regions by forming Pb–O bonds, among them laser modified region shows the highest concentration. Even though the perovskite single crystals are free of grain boundaries, they can be defective systems due to the non-uniform crystal growth direction and the formation of multiple seeds during the crystal growth (as shown by the perovskite crystal model in Fig. 1d (4)) [40]. Reduction of such intrinsic defect structures is mandatory for improving the optoelectronic properties of the perovskite materials. In general, these different regions can be defined relying on the distance from the center of the ablated crater, in this work: the ablated region <250 μm, 250 μm< the recast deposit region< 300 μm, 300 μm< the laser modified region< 500 μm, and the laser unaffected region >500 μm, respectively.

The elemental analyses through EDX demonstrated the surface chemistry modification of these four regions (shown in Figure S2). The Pb/Br atomic ratio gives clear information about the laser-induced modification on the $MAPbBr_3$ sample to cause $PbBr_2$ formation around the ablated crater, which determines the stability and optoelectronic behavior of the crystal. The atomic ratio of about 1:2.05 for the ablated region shows the possible damage that takes place in the region due to severe ablation. Thus, the region consists of almost pure $PbBr_2$ molten structures after the decomposition of the organic components in the sample. And the recast deposition region gives a Pb/Br ratio of about 1:2.7, which mainly resulted from the deposited $MAPbBr_3$ micro/nanostructures around the ablated crater. The measured atomic ratios of about 1:2.9 and 1:3.0 for the laser modified and unaffected regions, respectively, show the presence of almost pure crystalline $MAPbBr_3$ on the surface. The following section discusses the luminescence properties of laser ablated single crystal perovskite structures based on their surface chemistry and morphology.

2.2. PL and ASE behaviors of the laser processed SC perovskite

Usually, a steady-state PL analysis is closely correlated with the dominating recombination states in the perovskite materials. With the help of PL measurements, we explored different pathways of the radiative recombination mechanisms for each laser-induced region and the unaffected region on the $MAPbBr_3$ SC sample (the detailed explanation of the steady state PL measurement is given in the experimental section).

Fig. 2a shows the PL spectra from different laser affected and unaffected regions on the SC sample. A frequency-doubled femtosecond laser at the wavelength of 400 nm was employed as a pump beam, with a laser spot size of 0.09 mm^2 and a constant pump fluence of around 330 μJ/cm^2. In comparison to the measurement of the unaffected region, the observed peak positions from the laser modified region exhibit a clear blue shift, while the PL peaks from both the recast deposition and ablated regions show a considerable redshift. To find the reason for these asymmetric peak shifts, the pump dependent PL emission analysis was carried out for each region.

Figures S4 and S5 show the deconvolution of asymmetric PL emission peaks with multiple Gaussian functions. As shown in Fig. 2b, the appearing peak 2 of the unaffected and laser modified regions stand almost at the same position and exhibit a similar variation trend with increasing the pump fluence. This indicates that the emission associated with the peak 2 from these regions should be originated from a similar recombination source. Along with that, the results presented in Fig. 2c shows that the emission intensity from both the unaffected and laser modified regions began to saturate with increasing the pump fluence (like the trap filling effect). These results show that the peak 2 with a broad line width is originated from defect-like states with the limited density. As a result, the corresponding PL intensities became saturated as the photogenerated excessive carriers filled the available defect states [41].

On the other hand, the peak 1 of the laser modified region is significantly intense and blue-shifted when compared with the peak 1 of the unaffected region. It shows that we could effectively cure some of the defect-mediated recombination pathways via oxygen-mediated low intensity laser treatment. Thus, the dominant carrier recombination mechanisms in the region are mediated through the shallower optically active defect states or the free carrier band to band recombination mechanisms. Eventually, it helps to form a high-performance perovskite region with enhanced light emitting behavior. Our results show a good agreement with the previous reports [38,41].

Different from unaffected and laser modified regions, the measured PL emission intensities from the ablated region and the recrystallized nanocrystals at recast deposition regions show a monotonic increment when increasing the pump fluence (see Figure S6 and Fig. 3c). In the case of the ablated region, all the individual emission peak intensities are plotted against the corresponding pump fluences as a log-log plot (see Fig. 2c), in which the linear plots are fitted with a power law equation– $I_{emission} \sim (I_{pump})^k$, and the exponent corresponds to the slope of a curve. For the ablated peaks 1, 2, and 3, the measured slope values are m = 2.1, 1.7 and 2.0, respectively. The previous reports showed that the quadratic relationship between the $I_{emission}$ and I_{pump} can be used to confirm the excitonic radiative recombination mechanism [42]. Besides, the slope value of m = 2 with the large separation of peaks (~120 meV) indicates that the peaks originated from the bounded exciton (BE) recombination emission. Noticeably, the third peak shown in Fig. 2c is formed only for the pump fluence larger than 385 μJ/cm^2, which might correspond to the BE recombination with some newly formed laser induced defect states at higher pump intensities.

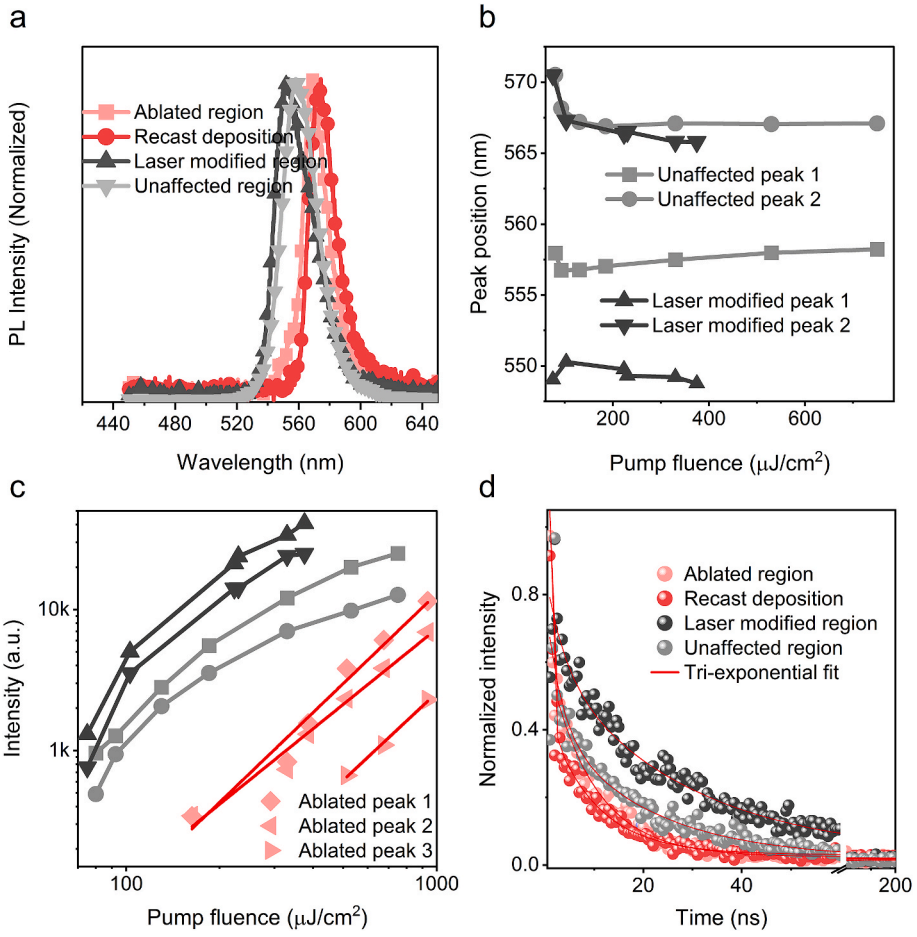

Fig. 2. Space-resolved PL emission analysis of the laser ablated SC $MAPbBr_3$. (a) A comparison of the measured PL spectra from the unaffected and different laser induced regions. (b) Variation of PL peak positions of the laser modified region and the unaffected region with different pump fluence. (c) Measured pumping fluence-dependent PL emission intensity of the unaffected region, laser modified region and ablated region at room temperature. The power-law equation was used to fit the peaks corresponding to the ablated region. The R^2 value of all three fittings is greater than 98.5%. (d) Measured TRPL decay response with the tri-exponential fitting for the different regions of the laser ablated $MAPbBr_3$ SC.

In the case of the recast deposition region, the pump fluence dependent-PL emission shows a clear enhancement in a non-linear fashion, which is clearly different behavior than the other regions. Upon pumping from the top, the pump beam seems to be effectively coupled into the abundant recrystallized perovskite micro/nano-structures (see Fig. 3a) to result in a strong PL emission. Noticeably, the optical cross-section images of these nanostructures show a clear luminescence emission enhancement after $F_{th} = 508$ μJ/cm^2 (see Fig. 3b). It shows that the rough micro-nano recrystallized structures in the region can enhance the scattering effects with high PL yield, which can continuously multiply the scattering light to generate the ASE or random lasing [38]. These two regimes are accurately differentiated by considering the line width and the growth of the output intensity (also called slope efficiency) after the lasing threshold. We here deconvoluted the obtained asymmetric PL peaks using two Gaussian functions (peak 1 and peak 2 shown in Fig. 3c). Interestingly, both the full-width-at-half-maximum (FWHM) and the intensity of the peak1 show a clear transition at the laser pumping fluence threshold of $F_{th} =$ 508 μJ/cm^2. After this threshold, the FWHM value of the peak1 is reduced from ~19 nm to ~11 nm, and the slope of the PL intensity growth is increased from $\eta = 1.57$ to 11.29. The results indicate that the emission corresponding to the peak 1 is moderately amplified after the threshold of $F_{th} = 508$ μJ/cm^2 (see Fig. 3d). Nevertheless, both a small slope efficiency and small FWHM reduction confirm that peak 1 should belong to the ASE-like emission rather than RL-like performance, the major reason for this might be the poor Q-factor of the recrystallized perovskite structures due to their highly rough morphology [43].

A recent study reported that the laser induced secondary crystallization can significantly enhance the photoluminescence properties of the perovskite materials by reducing the non-radiative recombination centers [38]. Based on this fact, there will be a higher chance of exciton-exciton and exciton-phonon interaction in the recrystallized nanostructures formed at the recast deposition region. Because of the strong Coulomb interaction among multi-excitons in perovskite nanostructures, the biexciton mechanism can be considered as the major gain mechanism that causes the ASE effect for the peak 1 [44]. On the other hand, both the relatively broad line width (FWHM ~30- 22 nm) and the absence of the sharp intensity growth for the peak 2 indicate that the corresponding emitted photons are not sufficiently amplified (see Figure S3). Furthermore, the peak 2 is separated by around 60 meV, which is greater than the typical energy difference happening through exciton-exciton scattering. Hence, this lower energy peak can be attributed to the BE from the exciton-phonon coupling via Coulomb interaction [42].

The dynamic PL analysis by TRPL measurement was carried out to explore the underlying recombination mechanisms in all the studied regions. The measured TRPL curves are fitted with a tri-exponential decay function of $I(t) = A_1exp(-t/\tau_1) + A_2exp(-t/\tau_2) + A_3exp(-t/\tau_3)$, in which the PL dynamics are considered as a combination of the fast (τ_1), medium (τ_2) and slow-decay (τ_3) processes, and the corresponding fractional contributions (f_1, f_2, f_3) can be obtained, as shown in Fig. 2d and Table S1. The average PL decay lifetimes ($\tau_{avg} = \tau_1 f_2 + \tau_2 f_1 + \tau_3 f_3$) for the ablated, recast deposition, laser modified, and unaffected regions are determined as 7.75 ns, 8.82 ns, 33.26 ns, and 19.14 ns, respectively. The longer lifetime for the laser modified region is attributed to the passivation of surface recombination centers by the lower intensity of the laser pulse tail in the presence of oxygen and moisture under laboratory conditions. Jointly with the high PL yield observation at the laser modified region, the long τ_{avg} indicates the low non-radiative defect density with the higher crystallinity among all other regions. Therefore, we can assume that the femtosecond laser modification can help to passivate or cure the defects by improving the crystalline properties of perovskite samples. In contrast, the ablated region with the maximum laser pulse energy deposition shows a poor PL yield and a short τ_{avg} compared to all other regions. The reason might be the dominant non-radiative recombination process mediated through both the surface and bulk defect densities that are caused by distorting the crystalline nature of the single-crystal perovskite sample. Similarly, the lower decay

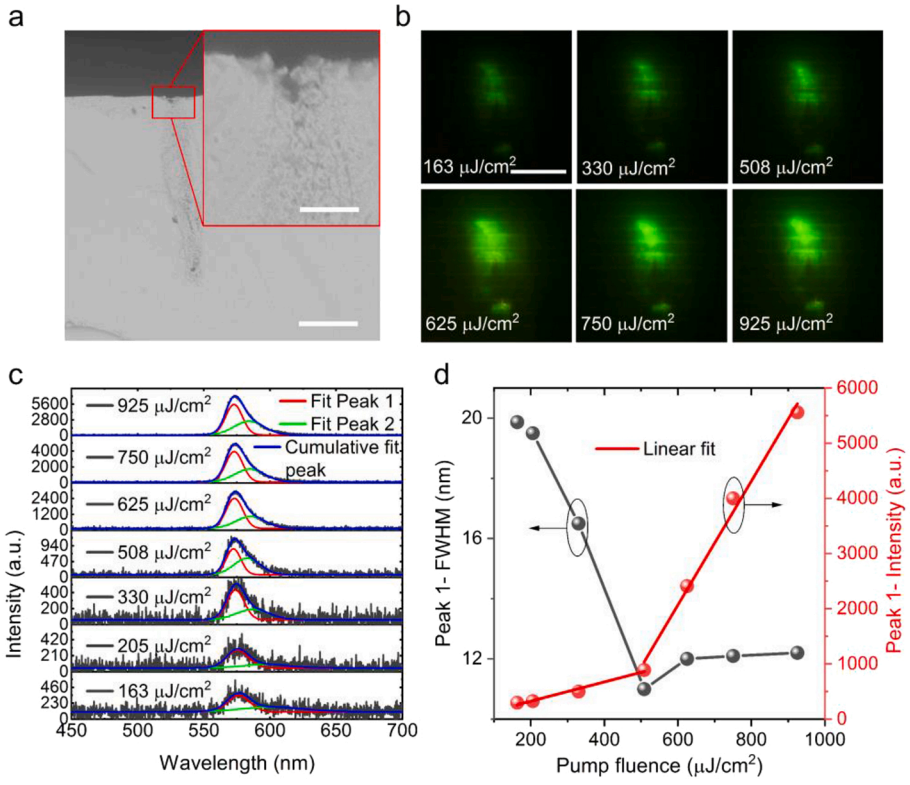

Fig. 3. ASE performance of recast deposition region of the SC $MAPbBr_3$. (a) A cross-section image of the ablated sample shows the fabricated structure beneath the sample surface (scale bar, 30 μm), where an inset picture for the magnified image of the irregular recrystallized random nanostructures (scale bare, 10 μm). (b) Series of optical images for the cross-section of the fabricated structure upon the optical pumping with different laser fluences (scale bare, 50 μm). (c) Measured PL spectrum of the recast deposit region on the perovskite single crystal sample with different pump fluences, in which all the asymmetric peaks are deconvoluted using two Gaussian peaks as the peak 1 and peak 2 (with an average R^2 value greater than 95%). (d) The pump fluence-dependent variations for the full-width-at-half-maximum (FWHM) and the intensity of the peak 1.

time constants associated with the unaffected region indicate a considerable amount of quick non-radiative recombination mediated through the defect states [45]. Therefore, the maximum defect passivation is needed for the bulk (3D) SC perovskites to avoid a large amount of intrinsic optical loss through the nonradiative emission. Similarly, the following sections will discuss the optical properties of $MAPbBr_3$ thin film across the laser-ablated microstructures.

2.3. Femtosecond laser processing of $MAPbBr_3$ thin films

In this experiment, the $MAPbBr_3$ PC sample was spin-coated on a glass substrate using a widely reported solvent engineering process (detailed information is given in the experimental section). The obtained film with a thickness of around 200 nm possessed a smooth surface consisting of a compact grain arrangement, as verified by the high-resolution SEM images (see Fig. 4a and b). Different from the ablation of the crater on $MAPbBr_3$ SC surface, we here produced the micro-strip patterns by scanning the femtosecond laser pulses across the thin film sample (the detailed information given in the experimental section). However, the crystalline modification over the laser processed structures will be similar to that of the single crystals (as shown by the perovskite crystal models in Fig. 4d–f).

A series of SEM images illustrate the surface morphology of the film sample induced by the high-repetition-rate (f_{treat} = 500 kHz) femtosecond laser irradiation. Fig. 4c shows parallel ablated strips on the thin film with the laser modified region (at a distance of tens of micrometers away from the ablated strip edge) and the unaffected region. At the ablated region, almost all the perovskite material was removed through the laser ablation and some melted $MAPbBr_3$ particles were left behind (see Fig. 4e). This might be due to the combined effect of the Gaussian-profiled laser pulse intensity and the structural/chemical inhomogeneity of the grain-to-grain boundary in the femtosecond laser energy propagation during the material processing. Owing to the Gaussian intensity distribution shown in Fig. 1a, the interaction of the low-intensity pulse tail with the samples takes place at a few micrometers near the ablated regions, such regions can be considered as the laser modified regions. Fig. 4d shows the unaffected region and the laser modified region, which correspond to the above and the below the dashed line, respectively. As there is no clear boundary between these two parts, we can assume that the area containing the large size of grains belongs to the former and the area containing a large number of smaller size grains along with abundant nano-holes (marked in Fig. 4d) belongs to the latter. As reported by

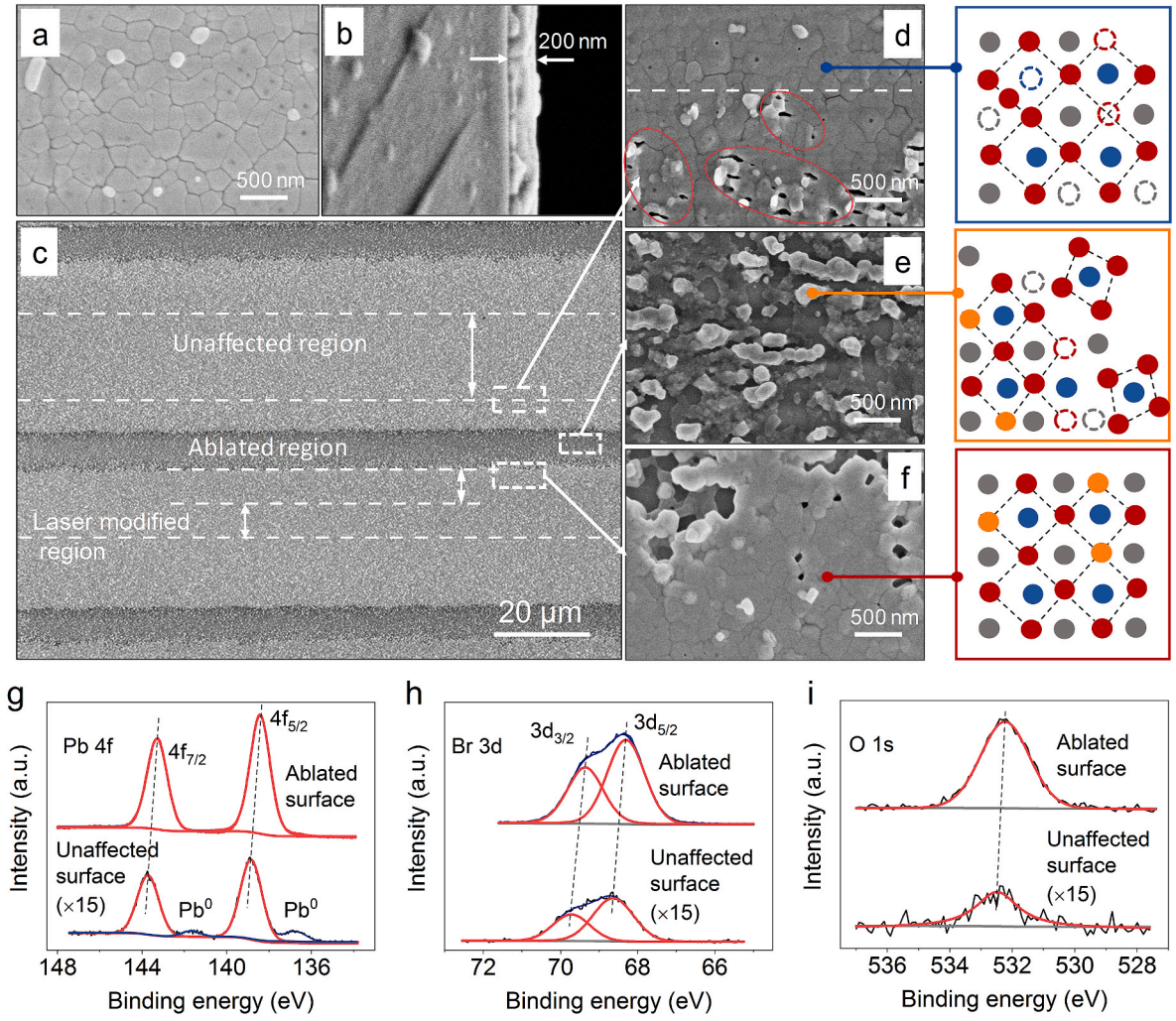

Fig. 4. Surface morphologies and chemistry of $MAPbBr_3$ PC thin film before and after the femtosecond laser ablation. (a) SEM image of the PC sample surface without femtosecond laser ablation, (b) Cross-section view of the bare sample surface to show the thickness of the thin film. (c) SEM images of the laser ablated microstrips. (d) Magnified image showing the unaffected region at the top and the laser modified region at the bottom, (e) the ablated region, and (f) the laser modified region with their corresponding crystal models (the graphics and their color used in these models are the same as we mentioned in Fig. 1d). (g–i) Measured XPS spectra of Pb 4f, Br 3 d and O 1s core levels for the laser unaffected and ablated regions, respectively. (For interpretation of the references to colour in this figure legend, the reader is referred to the Web version of this article.)

Bayer et al., such nano-holes are formed due to the removal of individual grains from the sample, which generally appears on the outside of the ablated structures (i.e, at the laser modified region), under the irradiation of the low-intensity laser pulse tail [46]. Besides, the grain size statistics for the unaffected and the laser modified regions confirm that the latter region consists of the noticeably smaller crystalline grains (see Figure S7).

In order to analyze the surface chemistry modifications before and after the laser ablation, we carried out the X-ray photoelectron spectroscopy (XPS) measurement of the unaffected and the ablated regions. Fig. 4(g–i) shows the XPS results with the variation of Pb 4f, Br 3 d, and O 1s core levels on the unaffected and ablated surface regions, which include the doublet spin-orbit coupling peaks of Pb $4f_{5/2}$ (at 143.4 eV) and $4f_{7/2}$ (at 138.5 eV) of Pb 4f and Br $3d_{3/2}$ (at 68.3 eV) and Br $3d_{5/2}$ (69.4 eV) of Br 3 d. The peak intensities for both Pb 4f and Br 3 d show a significant increment after the laser ablation, which indicates a large amount of $PbBr_2$ deposition on the sample surface due to the ablation process. Interestingly, as shown in Fig. 4g, the disappearance of metallic Pb (Pb^0) is accompanied by the lower energy shift and broad Pb^{2+} peak (at 138.5 eV). It demonstrated that the Pb^0 components undergo oxidization to Pb^{2+}, and the peak broadening observed is typical for metal oxide components. Simultaneously, increasing the intensity of the O 1s peak confirms a large amount of lead oxide (Pb–O) formation after the laser treatment. These results show that the Pb^0 is converted to Pb–O, i.e. heavy oxidative passivation under the laser treatment in the ambient atmosphere, which is a renowned mechanism behind the "photo-brightening" effect (increasing PL yield when irradiating under the ambient atmosphere) of perovskite materials [47,48].

As reported in the previous literature [49], the laser-induced thermal effects can promote $MAPbBr_3$ thin film sample to undergo degradation as follows:

$$CH_3NH_3PbBr_3 \rightarrow PbBr_2 + CH_3NH_2 + HBr \quad (1)$$

which shows the possible permanent decomposition of $MAPbBr_3$ thin films due to the formation of gaseous HBr and losing Br content. The heat accumulation effect upon irradiation of the high-repetition-rate laser pulses plays a major role in the thin film degradation at the laser ablated area. However, the UV–Vis absorption results in Figure S8 confirm that the optical properties around the laser processed area are still conserved.

2.4. PL and RL behaviors of the laser processed thin film perovskite

In order to evaluate the light-emitting behavior across the laser processed PC samples in detail, we spatially divided the ablation strip into three parts: the ablated region, the laser modified region, and the unaffected region. Then performed PL mapping and lasing experiments across these three regions to analyze the space-resolved luminescence behaviors. The recast deposition region appearing on the SC perovskite is not so prominent in the case of thin films. Fig. 5a and b shows the morphology of the laser-ablated microstrip on the thin film perovskite and the PL mapping result across this ablated stripe (as marked by the white line). The observation of PL emission around the ablated structure aligns with the surface morphology and chemistry analyses. Due to a large amount of $MAPbBr_3$ ablation from the center of the microstrip, a low PL intensity was observed. While compared to the PL yield at the unaffected region (the two ends of the PL intensity profile in Fig. 5b), the PL emission from the ablated region was blue shifted with four to five times smaller in intensity (see Fig. 5c). This blue shift was primarily due to the quantum confinement effect caused by the formation of $MAPbBr_3$ nanocrystals in the region [50]. Similar to the observation of enhanced PL yield from the laser modified region of the SC case, the edges of the laser ablated microstrip on the thin film perovskite exhibit the highest PL intensity than other regions. As mentioned before, the passivation of non-radiative defects under irradiation of low-intensity laser pulse tails in the presence of atmospheric oxygen might be responsible for the

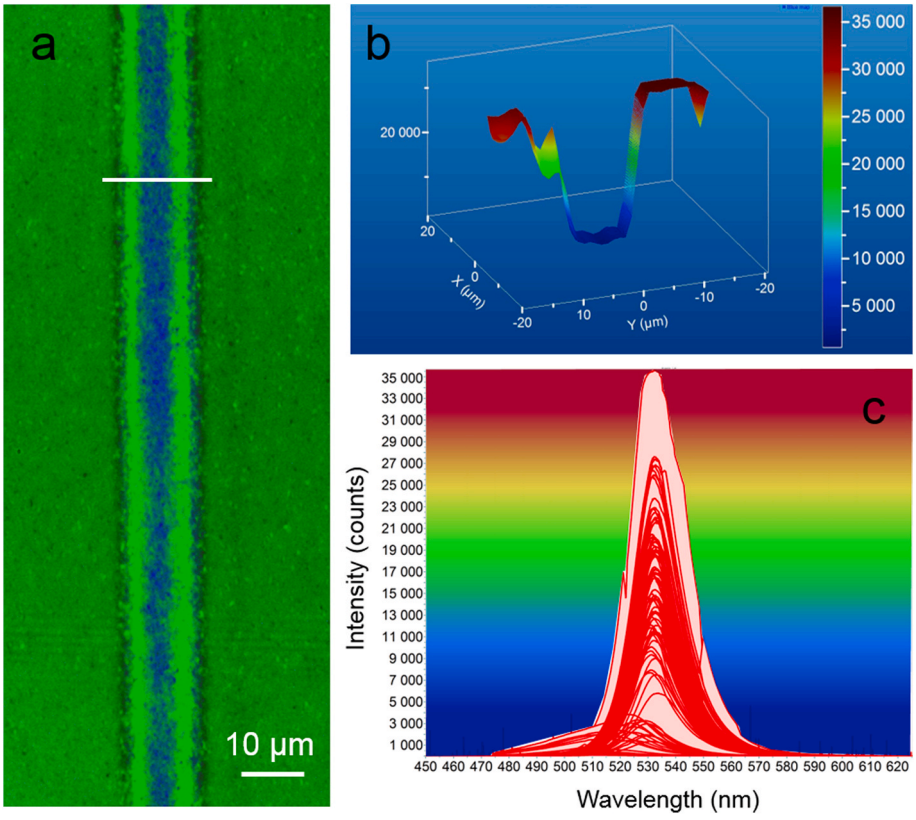

Fig. 5. (a) Morphology of the laser fabricated micro-strip on $MAPbBr_3$ PC thin film. (b) Measured photoluminescence mapping across the laser ablated strip, and (c) resultant PL spectra, the color gradient at the background indicates the corresponding groove position and PL intensity to (b).

resulting PL enhancement.

This section investigates the lasing performance of all three regions on the laser ablated $MAPbBr_3$ thin film. Numerous research works have already investigated the dependence of PL emission properties on the pumping energy for thin film perovskites [51–53], which point out the RL generation at the pumping energy above the lasing threshold due to the strong random scattering at the grain boundaries. As mentioned in the previous sections, the femtosecond laser ablation not only creates some novel micro and nanoscale features but also generates and cures various defect states in the perovskite samples to eventually modify the RL behavior. Here we characterize the emission of RL by selectively exciting the laser-affected and unaffected regions with a focused femtosecond laser (it is having a wavelength of $\lambda = 400$ nm and pulse width of $\tau_p = 40$ fs, see the experimental section for the detailed information). In order to avoid the pump laser-induced damage and the morphological change, we keep the pump laser energy density in the range of $F_{pump} = 1.0$ μJ/cm^2 to ~40.0 μJ/cm^2, which is much smaller than the reported damage threshold value (around >400 μJ/cm^2) of the $MAPbBr_3$ sample [49].

Primarily, we excited the unaffected region of the sample and characterized the emission behavior by slowly increasing the pump light fluence. Simultaneously, the PL emission was collected from the sample edge by using a multi-mode fiber attached to a high-resolution spectrometer. The measured pump fluence dependent PL spectra and the output emission intensity growth along with the spectrum line-width reduction are shown in Fig. 6a and b, respectively. The results clearly demonstrate that at the lower pump fluences, the spontaneous emission peaks tend to emerge at about 532 nm with the linewidth full width at half maximum (FWHM) of around 29 nm. At the pump fluence of $F_{pump} = 14.77$ μJ/cm^2, however, the PL emission peak becomes narrowed at 550 nm with the FWHM value of around 4.2 nm, and the peak intensity is rapidly increased for the further increment of the pump fluence. The lasing spectrum of the PC sample shows a global narrowing effect. Such a single RL peak of a few nm widths is either due to the long mean free path length of scattering light or by averaging out the interference effects formed while multiple scattering over a number of pumping laser shots [54], thus known as the incoherent RL. It can be explained by the well-known diffusion model with gain, in which interference effects are not taken into account [54]. The rapid growth of this lasing intensity with respect to the pump fluence gives a slope efficiency of $\eta = 1012$.

On the other hand, the story is a little bit different in the case of the ablated region. In the ablated region, direct femtosecond laser ablation process removed a majority of $MAPbBr_3$ grains and left a small number of recrystallized perovskite nanocrystals of just tens or hundreds of nm in size. Fig. 6c and d characterize the lasing emission from such nanocrystals at the ablated region, which gives the lasing threshold up to $F_{pump} = 20.00$ μJ/cm^2 and the slope efficiency of $\eta = 127$. Upon pumping of the highly intense femtosecond laser pulse, like the situation of SC perovskite nanocrystals, the RL emission from the ablated region of the PC sample is dominated by the bi-exciton recombination mechanism [38,44]. In comparison with the unaffected region, there observed a noticeable decrement in both the lasing threshold and the slope

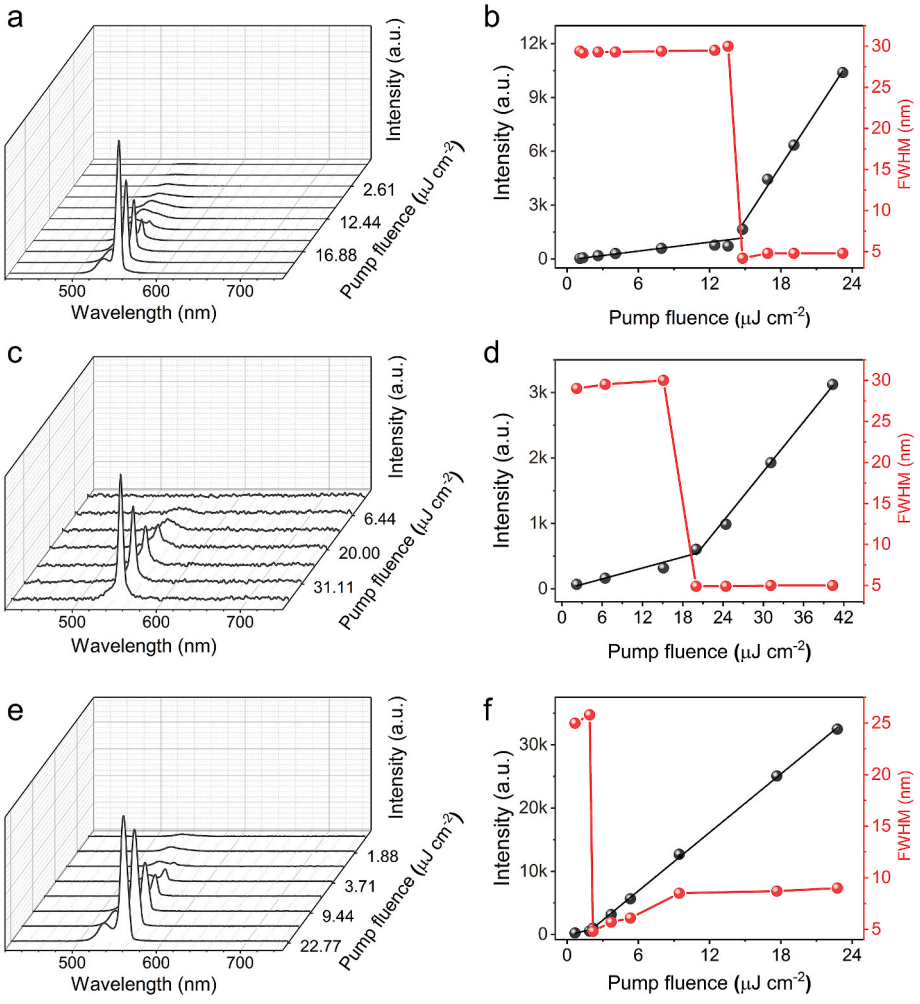

Fig. 6. Measured evolution of the RL behavior including the emission spectrum, peak intensity and the spectral FWHM width with respect to the pump fluence, where (a) and (b) denote situations of the unaffected region, (c) and (d) for the laser ablated region, (e) and (f) for the laser modified region.

efficiency. It can be attributed to a large amount of perovskite ablation from the region and the loss of excitons via the exciton-phonon coupling.

Interestingly, the lasing output from the laser modified region (see Fig. 6e and f) exhibits enhanced performance, such as the low lasing threshold of $F_{pump} = 2.17$ μJ/cm^2 and a high slope efficiency of $\eta = 1539$. It is noteworthy that the lasing threshold is reduced by 7 times and the slope efficiency is increased by 1.5 times than that of the unaffected region. This observation aligned well with the PL response of this region as discussed in the previous section. Hence, the improved intensity of lasing emission can be ascribed to the non-radiative defect passivation mediated by atmospheric oxygen under irradiation of low-intensity pulse trails. This kind of defect passivation would like to inhibit the quick non-radiative recombination pathways for the excited carriers and largely improve the light amplification process by the stimulated emission [55].

In addition, Figure S7 shows the grain size statistics of the unaffected and the laser modified regions. The average grain size in the unaffected region is reduced from around 220 nm to around 144 nm in laser modified region. Such grain size reduction can increase the surface randomness and significantly multiply the scattering effects. Therefore, the enhancement of random lasing behavior at the laser modified region is attributed to the smaller grain sizes and the laser-induced defect passivation with atmospheric oxygen. To the best of our knowledge, the lasing threshold exhibited by the laser modified region can be ranked among the top 10% of the lowest random lasing threshold that is reported with the perovskite materials [38,51,52,53,56,57].

3. Conclusion

In conclusion, we have investigated the PL, ASE and RL behaviors of the femtosecond laser ablated micro/nanostructures for both the SC and PC $MAPbBr_3$ perovskite samples, by spatially dividing them into the ablated, recast deposited, laser modified and unaffected regions with a tightly focused femtosecond laser beam. The nonlinear interaction of intense laser pulses was found to induce the space resolved material chemistry and sample morphology, which causes different carrier recombination mechanisms. It was observed that upon the femtosecond laser ablation, the recrystallized micro/nanostructures formed on the SC surface exhibit the ASE. In the case of PC samples, owing to the laser induced non-radiative defect passivation and the reduction of average crystalline grain sizes by more than 1.5 times, a significant enhancement of incoherent RL behavior was evidenced (the RL threshold was reduced by seven times and the slope efficiency increased by ~1.5 times). Through this study, we can clearly understand how the light emitting and lasing behaviors of both the single crystal and thin film perovskites are affected by the femtosecond laser induced surface morphology and defect states. It is believed that our findings will lay a solid foundation for fabricating the desired perovskite light-emitting microstructures using highly scalable and automated femtosecond laser processing methods.

4. Experimental methods

4.1. Perovskite synthesis

Chemicals: *N*,*N*-Dimethylformamide (DMF) (99%) was purchased from Sigma-Aldrich Ltd. Methylammonium bromine (MABr, 99%) and Lead bromine ($PbBr_2$, 99%) were purchased from Xi'an Polymer Light Technology Corp. Silicone oil was purchased from Aladdin Reagent Ltd. All the chemicals were used as received without further purification.

Synthesis of $MAPbBr_3$ SCs: 15 mmol MABr and 15 mmol $PbBr_2$ were dissolved in 10 mL DMF to creat 1.5 mol/L $MAPbBr_3$ solution. The solution needs to be stirred in nitrogen for 24 h to ensure full dissolution. After stirring, the glass bottle containing the solution was soaked into the silicone oil at room temperature. Then the silicone oil was heated by 2° per hour until 70 °C. Some small crystal seeds gradually precipitate in the solution. Keep the silicone oil 70° for a day and the crystal grows to acentimeter level. Then removed the solution bottle from the silicone oil, clamped the crystal out of the solution with tweezers, and dried the residual solution on the surface.

Synthesis of $MAPbBr_3$ PCs: The precursor solution for $MAPbBr_3$ was prepared by dissolving Methylammonium bromide (MABr, 1 mmol, 112 mg) and $PbBr_2$ (1 mmol, 376 mg) in 1 mL of co-solvent that is prepared by taking the volume ratio of dimethyl sulfoxide (DMSO) and γ-butyrolactone (GBL) as 1:1. Here, the plasma cleaned glass substrates were used as the substrates for the two step spin coating method used to coat the perovskite precursor solution, which was carried out at 1000 and 5000 rpm for 10 and 20 s, respectively, and at 17s with 5000 rpm, the wet spinning film was quenched by dropping 50 μL of anhydrous toluene into a glove box filled with nitrogen (>99.999%). All the films were annealed sequentially at 75, 95, 115, and 135 °C for 10 min after the spin coating process.

4.2. Femtosecond laser processing

SC $MAPbBr_3$ sample processing: A high repetition rate laser beam of f_{treat} = 500 kHz, λ = 1030 nm and average power of 600 mW is irradiated normally on the sample for less than 2 s duration. A focal lens of $f = 200$ mm was used to focus the laser beam exactly on the surface of the SC sample. Subsequent surface morphology analyses confirmed that a crater of around 500 μm diameter and 240 μm depth was formed through the ablation mechanism.

Thin film $MAPbBr_3$ sample processing: Here we used a similar laser source as above, the laser beam of an average power of 600 mW is focused normally onto thin film sample placed on an X-Y-Z stage, of micrometer precision for translating the sample. This X-Y-Z translation stage was fully controlled by a computer program. The stage was adjusted in the Z-direction for keeping the sample at the laser beam focus spot. The parallel ablated strips were fabricated by moving the sample across the focal spot at a speed of 2.5 mm/s.

4.3. XPS measurement

The surface electronic properties of $MAPbBr_3$ thin film samples were characterized by acquiring a full XPS spectrum using Thermo Scientific, Escalab 250 Xi, monochromated Al Kα- 1486.6 eV source with the detection depth of less than 10 nm. The BE scale of all the studied spectra was calibrated using the carbon peak at ~284.8 eV as a reference. The acquisition time for each scan was ~40 s. Peak fittings and analyses were carried out with the XPS peak 41 software. Because of the inelastic scattering processes, the Shirley function was used to define the background signal. The raw spectrum data of all the peaks were fitted with Gaussian-Lorentzian functions. All the important spectrum features such as peak positions, full width at half maximum (FWHM) and peak areas were calculated from the fitted sub-peaks.

4.4. PL measurement

SC $MAPbBr_3$ sample: The frequency-doubled femtosecond laser beam of 400 nm with the laser spot size of 0.09 mm^2 was employed to measure the PL. This beam was generated by transmitting an input beam operating at 800 nm with 40 fs pulses and a repetition rate of 1 kHz through a phase-matched BBO crystal. The sample was excited normally after confirming the region of interest by using a CCD camera. Subsequently, the emission output (PL) was collected using a high numerical aperture objective lens and focused on a multimode optical fibre connected with high resolution spectrometer for further analysis. All the measurements were taken in ambient conditions.

PC $MAPbBr_3$ sample: The PL mapping across the laser-ablated microstrip was carried out with a HORIBA Scientific Raman Spectrometer at 473 nm continuous wave laser with 2.55 mW/cm^2 laser intensity in the ambient conditions.

4.5. TRPL measurement

The TRPLs of bare and laser-treated $MAPbBr_3$ thin films were measured by means of a home-built confocal microscope. A pulsed supercontinuum laser (OYSL Photonics, *S*C-Pro, 150 ps pulse lengths) at a 2 MHz repetition rate was used as the laser source. The focused pump laser of 532 nm irradiated the sample through an objective lens of N.A. = 0.4 with the power ~0.132 μW. A long-pass filter with a 532 nm edge (Semrock) was used to filter out the pump scattered light from the pump laser to the detector. The photoluminescence from the samples was detected by a SPCM-AQRH single photon counting module (SPCM-AQRH-15, Excelitas Technologies), and the lifetime module was TimeHarp 260 P (PicoQuant).

4.6. Lasing experiment

An optical pumping setup constructed with the femtosecond laser beam pulse trains at the repetition rate of 1 kHz with a time duration of 40 fs was used to perform the RL experiments of samples before and after laser treatments. All the lasing experiments were conducted at room temperature in a dark box, with anti-reflective walls. The femtosecond laser system used for the optical pumping is the same as the one used for laser treatment (as mentioned above). An external frequency-doubling beta barium borate (BBO) crystal was used to obtain the second harmonic wavelength of 400 nm, which is in the absorbance region of $MAPbBr_3$. For the optical pumping, the beam of ~10 mm diameter was focused normally on the thin film samples by a cylindrical lens with a focal length of 75 mm. To avoid the influence of self-absorption losses, the distance between the pumping strip and the sample edge was almost zero. Simultaneously, the lasing output from the edge of the sample was directly collected using a multi-mode optical fiber and fed to a spectrometer (Ocean optics USB 4000) for observing the output spectrum.

Credit author statement

Rahul A. Rajan: Conceptualization, Methodology, Verification, Formal analysis, Investigation, Writing – Original Draft, Writing – Review & Editing. **Huang Tao:** Verification, Resources, Investigation, Writing – Review & Editing. **Weili Yu:** Conceptualization, Supervision, Writing – Review & Editing. **Jianjun Yang:** Conceptualization, Supervision, Writing – Review & Editing, Project administration, Funding acquisition.

Declaration of competing interest

The authors declare that they have no known competing financial interests or personal relationships that could have appeared to influence the work reported in this paper.

Data availability

Data will be made available on request.

Acknowledgment

The authors acknowledge Wenchi Kong for the preparation of experimental samples and Yucai Lin for measuring the UV–vis absorption spectra. This research was financially supported by the National Natural Science Foundation of China (Grant Nos. 91750205, 11674178), Strategic Priority Research Program of Chinese Academy of Sciences (Grant No. XDA22010302), Jilin Provincial Science & Technology Development Project (Grant No. 20200201086JC), and Rahul A. Rajan gratefully acknowledge his support from UCAS Full-Fellowship for International Students (20190442).

Appendix A. Supplementary data

Supplementary data to this article can be found online at https://doi.org/10.1016/j.mtphys.2023.101000.

References

[1] X. Guan, T. Wan, L. Hu, C.H. Lin, J. Yang, J.K. Huang, C.Y. Huang, S. Shahrokhi, A. Younis, K. Ramadass, K. Liu, A. Vinu, J. Yi, D. Chu, T. Wu, A solution-processed all-perovskite memory with dual-band light response and tri-mode operation, Adv. Funct. Mater. 32 (2022), https://doi.org/10.1002/adfm.202110975.

[2] W. Yu, F. Li, L. Yu, M.R. Niazi, Y. Zou, D. Corzo, A. Basu, C. Ma, S. Dey, M.L. Tietze, U. Buttner, X. Wang, Z. Wang, M.N. Hedhili, C. Guo, T. Wu, A. Amassian, Single crystal hybrid perovskite field-effect transistors, Nat. Commun. 9 (2018) 1–10, https://doi.org/10.1038/s41467-018-07706-9.

[3] Y. Miao, L. Cheng, W. Zou, L. Gu, J. Zhang, Q. Guo, Q. Peng, M. Xu, Y. He, S. Zhang, Y. Cao, R. Li, N. Wang, W. Huang, J. Wang, Microcavity top-emission perovskite light-emitting diodes, Light Sci. Appl. 9 (2020), https://doi.org/10.1038/s41377-020-0328-6.

[4] Q. Shan, C. Wei, Y. Jiang, J. Song, Y. Zou, L. Xu, T. Fang, T. Wang, Y. Dong, J. Liu, B. Han, F. Zhang, J. Chen, Y. Wang, H. Zeng, Perovskite light-emitting/detecting bifunctional fibres for wearable LiFi communication, Light Sci. Appl. 9 (2020), https://doi.org/10.1038/s41377-020-00402-8.

[5] D. Zhang, Y. Fu, H. Zhan, C. Zhao, X. Gao, C. Qin, L. Wang, Suppressing thermal quenching via defect passivation for efficient quasi-2D perovskite light-emitting diodes, Light Sci. Appl. 11 (2022) 69, https://doi.org/10.1038/s41377-022-00761-4.

[6] Y.C. Zhao, W.K. Zhou, X. Zhou, K.H. Liu, D.P. Yu, Q. Zhao, Quantification of light-enhanced ionic transport in lead iodide perovskite thin films and its solar cell applications, Light Sci. Appl. 6 (2017) e16243–e16248, https://doi.org/10.1038/lsa.2016.243.

[7] S. Mahesh, B. Chen, E.H. Sargent, All-perovskite tandems go bifacial, Light Sci. Appl. 12 (2023) 13–14, https://doi.org/10.1038/s41377-022-01057-3.

[8] L. Zhang, C. Sun, T. He, Y. Jiang, J. Wei, Y. Huang, M. Yuan, High-performance quasi-2D perovskite light-emitting diodes: from materials to devices, Light Sci. Appl. 10 (2021) 61, https://doi.org/10.1038/s41377-021-00501-0.

[9] H. Li, Y. Wang, H. Gao, M. Zhang, R. Lin, P. Wu, K. Xiao, H. Tan, Revealing the output power potential of bifacial monolithic all-perovskite tandem solar cells, ELight 2 (2022), https://doi.org/10.1186/s43593-022-00028-w.

[10] N. Yantara, S. Bhaumik, F. Yan, D. Sabba, H.A. Dewi, N. Mathews, P.P. Boix, H. V. Demir, S. Mhaisalkar, Inorganic halide perovskites for efficient light-emitting diodes, J. Phys. Chem. Lett. 6 (2015) 4360–4364, https://doi.org/10.1021/acs.jpclett.5b02011.

[11] M. Roknuzzaman, C. Zhang, K. (Ken) Ostrikov, A. Du, H. Wang, L. Wang, T. Tesfamichael, Electronic and optical properties of lead-free hybrid double perovskites for photovoltaic and optoelectronic applications, Sci. Rep. 9 (2019) 1–7, https://doi.org/10.1038/s41598-018-37132-2.

[12] P. Papagiorgis, A. Manoli, L. Protesescu, C. Achilleos, M. Violaris, K. Nicolaides, T. Trypiniotis, M.I. Bodnarchuk, M.V. Kovalenko, A. Othonos, G. Itskos, Efficient optical amplification in the nanosecond regime from formamidinium lead iodide nanocrystals, ACS Photonics 5 (2018) 907–917, https://doi.org/10.1021/acsphotonics.7b01159.

[13] A. Younis, C.H. Lin, X. Guan, S. Shahrokhi, C.Y. Huang, Y. Wang, T. He, S. Singh, L. Hu, J.R.D. Retamal, J.H. He, T. Wu, Halide perovskites: a new era of solution-processed electronics, Adv. Mater. 33 (2021) 1–34, https://doi.org/10.1002/adma.202005000.

[14] K.J. Singh, X. Fan, A.S. Sadhu, C.-H. Lin, F.-J. Liou, T. Wu, Y.-J. Lu, J.-H. He, Z. Chen, T. Wu, H.-C. Kuo, CsPbBr 3 perovskite quantum-dot paper exhibiting a highest 3 dB bandwidth and realizing a flexible white-light system for visible-light communication, Photon. Res. 9 (2021) 2341, https://doi.org/10.1364/prj.434270.

[15] A.Y. Zhizhchenko, P. Tonkaev, D. Gets, A. Larin, D. Zuev, S. Starikov, E. V. Pustovalov, A.M. Zakharenko, S.A. Kulinich, S. Juodkazis, A.A. Kuchmizhak, S. V. Makarov, Light-emitting nanophotonic designs enabled by ultrafast laser processing of halide perovskites, Small 16 (2020) 1–11, https://doi.org/10.1002/smll.202000410.

[16] C.W. Wang, Y.Y. Dang, Y.H. Su, J.C. Ni, C.C. Zhang, J.W. Li, Y.L. Hu, J.R. Chu, W. H. Huang, D. Wu, X.T. Tao, Femtosecond laser direct ablating micro/nanostructures and micropatterns on CH3NH3PbI3 single crystal, IEEE Photonics J 9 (2017) 1–10, https://doi.org/10.1109/JPHOT.2017.2676353.

[17] T. Zou, B. Zhao, W. Xin, Y. Wang, B. Wang, X. Zheng, H. Xie, Z. Zhang, J. Yang, C. L. Guo, High-speed femtosecond laser plasmonic lithography and reduction of graphene oxide for anisotropic photoresponse, Light Sci. Appl. 9 (2020), https://doi.org/10.1038/s41377-020-0311-2.

[18] F. Flamini, L. Magrini, A.S. Rab, N. Spagnolo, V. D'Ambrosio, P. Mataloni, F. Sciarrino, T. Zandrini, A. Crespi, R. Ramponi, R. Osellame, Thermally reconfigurable quantum photonic circuits at telecom wavelength by femtosecond laser micromachining, Light Sci. Appl. 4 (2015) 1–7, https://doi.org/10.1038/lsa.2015.127.

[19] Y.L. Sun, W.F. Dong, L.G. Niu, T. Jiang, D.X. Liu, L. Zhang, Y.S. Wang, Q.D. Chen, D.P. Kim, H.B. Sun, Protein-based soft micro-optics fabricated by femtosecond laser direct writing, Light Sci. Appl. 3 (2014) 1–7, https://doi.org/10.1038/lsa.2014.10.

[20] Z. Zhou, X. Ou, Y. Fang, E. Alkhazraji, R. Xu, Y. Wan, Prospects and applications of on - chip lasers, ELight (2023) 1–25, https://doi.org/10.1186/s43593-022-00027-x.

[21] H. Dong, C. Ran, W. Gao, M. Li, Y. Xia, W. Huang, Metal Halide Perovskite for next - generation optoelectronics : progresses and prospects, ELight (2023), https://doi.org/10.1186/s43593-022-00033-z.
[22] A. Zhizhchenko, S. Syubaev, A. Berestennikov, A. V Yulin, A. Por, A. Pushkarev, I. Shishkin, K. Golokhvast, A.A. Bogdanov, A.A. Zakhidov, A.A. Kuchmizhak, Y. S. Kivshar, S. V Makarov, Single-mode lasing from imprinted halide- perovskite microdisks, ACS Nano (2019), https://doi.org/10.1021/acsnano.8b08948.
[23] R. Fang, A. Vorobyev, C. Guo, Direct visualization of the complete evolution of femtosecond laser-induced surface structural dynamics of metals, Light Sci. Appl. 6 (2017) e16256–e16257, https://doi.org/10.1038/lsa.2016.256.
[24] H. Liu, W. Lin, M. Hong, Hybrid laser precision engineering of transparent hard materials: challenges, solutions and applications, Light Sci. Appl. 10 (2021), https://doi.org/10.1038/s41377-021-00596-5.
[25] P. Mao, C. Liu, X. Li, M. Liu, Q. Chen, M. Han, S.A. Maier, E.H. Sargent, S. Zhang, Single-step-fabricated disordered metasurfaces for enhanced light extraction from LEDs, Light Sci. Appl. 10 (2021), https://doi.org/10.1038/s41377-021-00621-7.
[26] Y. Fu, H. Zhu, C.C. Stoumpos, Q. Ding, J. Wang, M.G. Kanatzidis, X. Zhu, S. Jin, Broad wavelength tunable robust lasing from single-crystal nanowires of cesium lead halide perovskites (CsPbX3, X = Cl, Br, I), ACS Nano 10 (2016) 7963–7972, https://doi.org/10.1021/acsnano.6b03916.
[27] S. Enomoto, T. Tagami, Y. Ueda, Y. Moriyama, K. Fujiwara, S. Takahashi, K. Yamashita, Drastic transitions of excited state and coupling regime in all-inorganic perovskite microcavities characterized by exciton/plasmon hybrid natures, Light Sci. Appl. 11 (2022) 26–28, https://doi.org/10.1038/s41377-021-00701-8.
[28] B. Fazio, P. Artoni, M.A. Iat, C. D'Andrea, M.J. Lo Faro, S. Del Sorbo, S. Pirotta, P. G. Gucciardi, P. Musumeci, C.S. Vasi, R. Saija, M. Galli, F. Priolo, A. Irrera, Strongly enhanced light trapping in a two-dimensional silicon nanowire random fractal array, Light Sci. Appl. 5 (2016) 1–7, https://doi.org/10.1038/lsa.2016.62.
[29] E.Y. Tiguntseva, I.N. Saraeva, S.I. Kudryashov, E.V. Ushakova, F.E. Komissarenko, A.R. Ishteev, A.N. Tsypkin, R. Haroldson, V.A. Milichko, D.A. Zuev, S.V. Makarov, A.A. Zakhidov, Laser post-processing of halide perovskites for enhanced photoluminescence and absorbance, J. Phys. Conf. Ser. 917 (2017), https://doi.org/10.1088/1742-6596/917/6/062002.
[30] W. Yuan, R. Pang, S. Wang, T. Tan, C. Li, C. Wang, H. Zhang, Enhanced blue-light excited cyan-emitting persistent luminescence of BaLu2Al2Ga2SiO12:Ce3+, Bi3+ phosphors for AC-LEDs via defect modulation, Light Sci. Appl. 11 (2022), https://doi.org/10.1038/s41377-022-00868-8.
[31] K. Sugioka, Y. Cheng, Ultrafast lasers-reliable tools for advanced materials processing, Light Sci. Appl. 3 (2014) 1–12, https://doi.org/10.1038/lsa.2014.30.
[32] M. Malinauskas, A. Žukauskas, S. Hasegawa, Y. Hayasaki, V. Mizeikis, R. Buividas, S. Juodkazis, Ultrafast laser processing of materials: from science to industry, Light Sci. Appl. 5 (2016) 3–5, https://doi.org/10.1038/lsa.2016.133.
[33] S.D. Dane, W. deQuilettes, Sarah M. Vorpahl, H. Nagaoka, G.E. Eperon, M.E. Ziffer, J. Henry, Impact of microstructure on local carrier lifetime in perovskite solar cells, Sci. Express 33 (2015) 1–8, sciencemag.org/content/early/recent/).
[34] J. Xing, X. Zheng, Z. Yu, Y. Lei, L. Hou, Y. Zou, C. Zhao, B. Wang, Dramatically enhanced photoluminescence from femtosecond laser induced micro-/nanostructures on MAPbBr 3 single crystal surface, Adv. Opt. Mater. 1800411 (2018) 1–9, https://doi.org/10.1002/adom.201800411.
[35] S.M. Eaton, H. Zhang, P.R. Herman, F. Yoshino, L. Shah, J. Bovatsek, A.Y. Arai, Heat accumulation effects in femtosecond laser-written waveguides with variable repetition rate, Opt Express 13 (2005) 4708, https://doi.org/10.1364/opex.13.004708.
[36] C. Momma, S. Nolte, B. Chichkov, A. Tuennermann, F. von Alvensleben, Precise laser ablation with ultra-short pulses, Conf. Lasers Electro-Optics Eur. - Tech. Dig. 318 (1996), https://doi.org/10.1109/cleoe.1996.562552.
[37] C.S.R. Nathala, A. Ajami, W. Husinsky, B. Farooq, S.I. Kudryashov, A. Daskalova, I. Bliznakova, A. Assion, Ultrashort laser pulse ablation of copper, silicon and gelatin: effect of the pulse duration on the ablation thresholds and the incubation coefficients, Appl. Phys. Mater. Sci. Process 122 (2016) 1–8, https://doi.org/10.1007/s00339-016-9625-6.
[38] Y. Shi, R. Li, G. Yin, X. Zhang, X. Yu, B. Meng, Z. Wei, R. Chen, Laser-induced secondary crystallization of CsPbBr3 perovskite film for robust and low threshold amplified spontaneous emission, Adv. Funct. Mater. 2207206 (2022) 1–9, https://doi.org/10.1002/adfm.202207206.
[39] L. Huang, Z. Ge, X. Zhang, Y. Zhu, Oxygen-induced defect-healing and photo-brightening of halide perovskite semiconductors: science and application, J. Mater. Chem. A. 9 (2021) 4379–4414, https://doi.org/10.1039/d0ta10946k.
[40] Y. Lei, Y. Chen, R. Zhang, Y. Li, Q. Yan, S. Lee, Y. Yu, H. Tsai, W. Choi, K. Wang, Y. Luo, Y. Gu, X. Zheng, C. Wang, C. Wang, H. Hu, Y. Li, B. Qi, M. Lin, Z. Zhang, S. A. Dayeh, M. Pharr, D.P. Fenning, Y.H. Lo, J. Luo, K. Yang, J. Yoo, W. Nie, S. Xu, A fabrication process for flexible single-crystal perovskite devices, Nature 583 (2020) 790–795, https://doi.org/10.1038/s41586-020-2526-z.
[41] D. Priante, I. Dursun, M.S. Alias, D. Shi, V.A. Melnikov, T.K. Ng, O.F. Mohammed, O.M. Bakr, B.S. Ooi, The recombination mechanisms leading to amplified spontaneous emission at the true-green wavelength in CH3NH3PbBr3 perovskites, Appl. Phys. Lett. 106 (2015) 1–5, https://doi.org/10.1063/1.4913463.
[42] J. Shi, Y. Li, J. Wu, H. Wu, Y. Luo, D. Li, J.J. Jasieniak, Q. Meng, Exciton character and high-performance stimulated emission of hybrid lead bromide perovskite polycrystalline film, Adv. Opt. Mater. 8 (2020), https://doi.org/10.1002/adom.201902026.
[43] A.O. Murzin, B.V. Stroganov, C. Günnemann, S. Ben Hammouda, A.V. Shurukhina, M.S. Lozhkin, A.V. Emeline, Y.V. Kapitonov, Amplified spontaneous emission and random lasing in MAPbBr3 halide perovskite single crystals, Adv. Opt. Mater. 8 (2020) 1–5, https://doi.org/10.1002/adom.202000690.
[44] G. Nagamine, J.O. Rocha, L.G. Bonato, A.F. Nogueira, Z. Zaharieva, A.A.R. Watt, C. H. De Brito Cruz, L.A. Padilha, Two-photon absorption and two-photon-induced gain in perovskite quantum dots, J. Phys. Chem. Lett. 9 (2018) 3478–3484, https://doi.org/10.1021/acs.jpclett.8b01127.
[45] J. Xing, C. Zhao, Y. Zou, W. Kong, Z. Yu, Y. Shan, Q. Dong, D. Zhou, W. Yu, C. Guo, Modulating the optical and electrical properties of MAPbBr3 single crystals via voltage regulation engineering and application in memristors, Light Sci. Appl. 9 (2020) 111, https://doi.org/10.1038/s41377-020-00349-w.
[46] L. Bayer, X. Ye, P. Lorenz, K. Zimmer, Studies on perovskite film ablation and scribing with ns-, ps- and fs-laser pulses, Appl. Phys. Mater. Sci. Process 123 (2017) 1–8, https://doi.org/10.1007/s00339-017-1234-5.
[47] E.J. Juarez-perez, Photodecomposition and thermal decomposition in methylammonium halide lead perovskites and inferred design principles to increase photovoltaic device stability, J. Mater. Chem. A. 6 (2018) 9604–9612, https://doi.org/10.1039/c8ta03501f.
[48] J.S.W. Godding, A.J. Ramadan, Y.H. Lin, K. Schutt, H.J. Snaith, B. Wenger, Oxidative passivation of metal halide perovskites, Joule 3 (2019) 2716–2731, https://doi.org/10.1016/j.joule.2019.08.006.
[49] M.L. De Giorgi, T. Lippolis, N.F. Jamaludin, C. Soci, A. Bruno, M. Anni, Origin of Ampli Fi Ed Spontaneous Emission Degradation in MAPbBr 3 Thin Films under Nanosecond-UV Laser Irradiation, 2020, https://doi.org/10.1021/acs.jpcc.0c02331.
[50] V.I. Klimov, A.A. Mikhailovsky, S. Xu, A. Malko, J.A. Hollingsworth, C. A. Leatherdale, H.J. Eisler, M.G. Bawendi, Optical gain and stimulated emission in nanocrystal quantum dots, Science 290 (80-) (2000) 314–317, https://doi.org/10.1126/science.290.5490.314.
[51] Y.C. Wang, H. Li, Y.H. Hong, K. Bin Hong, F.C. Chen, C.H. Hsu, R.K. Lee, C. Conti, T.S. Kao, T.C. Lu, Flexible organometal-halide perovskite lasers for speckle reduction in imaging projection, ACS Nano 13 (2019) 5421–5429, https://doi.org/10.1021/acsnano.9b00154.
[52] T.S. Kao, Y.H. Chou, K. Bin Hong, J.F. Huang, C.H. Chou, H.C. Kuo, F.C. Chen, T. C. Lu, Controllable lasing performance in solution-processed organic-inorganic hybrid perovskites, Nanoscale 8 (2016) 18483–18488, https://doi.org/10.1039/c6nr05561c.
[53] S.P. Mallick, Y.H. Hong, L.R. Chen, T.S. Kao, T.C. Lu, Effect of passivation layer on the thin film perovskite random lasers, Materials 13 (2020), https://doi.org/10.3390/ma13102322.
[54] D.S. Wiersma, The physics and applications of random lasers, Nat. Phys. 4 (2008) 359–367, https://doi.org/10.1038/nphys971.
[55] G. Xing, N. Mathews, S.S. Lim, N. Yantara, X. Liu, D. Sabba, M. Grätzel, S. Mhaisalkar, T.C. Sum, Low-temperature solution-processed wavelength-tunable perovskites for lasing, Nat. Mater. 13 (2014) 476–480, https://doi.org/10.1038/nmat3911.
[56] Y.H. Hong, T.S. Kao, Room-temperature random lasing of metal-halide perovskites: via morphology-controlled synthesis, Nanoscale Adv. 2 (2020) 5833–5840, https://doi.org/10.1039/d0na00794c.
[57] A. Safdar, Y. Wang, T.F. Krauss, Random lasing in solution-processed perovskite thin films, Opt Express 26 (2018) 6623–6630, https://doi.org/10.1109/cleoe-eqec.2017.8087828.